

Efficient linear-scaling quantum transport calculations on graphics processing units and applications on electron transport in graphene

Zheyong Fan*, Andreas Uppstu, Topi Siro, Ari Harju

COMP Centre of Excellence and Helsinki Institute of Physics, Department of Applied Physics, Aalto University, Helsinki, Finland

Abstract

We implement, optimize, and validate the linear-scaling Kubo-Greenwood quantum transport simulation on graphics processing units by examining resonant scattering in graphene. We consider two practical representations of the Kubo-Greenwood formula: a Green-Kubo formula based on the velocity auto-correlation and an Einstein formula based on the mean square displacement. The code is fully implemented on graphics processing units with a speedup factor of up to 16 (using double-precision) relative to our CPU implementation. We compare the kernel polynomial method and the Fourier transform method for the approximation of the Dirac delta function and conclude that the former is more efficient. In the ballistic regime, the Einstein formula can produce the correct quantized conductance of one-dimensional graphene nanoribbons except for an overshoot near the band edges. In the diffusive regime, the Green-Kubo and the Einstein formalisms are demonstrated to be equivalent. A comparison of the length-dependence of the conductance in the localization regime obtained by the Einstein formula with that obtained by the non-equilibrium Green's function method reveals the challenges in defining the length in the Kubo-Greenwood formalism at the strongly localized regime.

Keywords: graphene, Quantum transport, Kubo-Greenwood formula, Chebyshev polynomial expansion, Graphics processing unit, CUDA

1. Introduction

Quantum simulations are very important tools to study transport phenomena in the nanoscale, both for electrons and phonons. There are mainly two numerical approaches for quantum transport simulations, one is the widely used non-equilibrium Green's function (NEGF) method [1] and the other is the Kubo-Greenwood method [2, 3]. Both methods have been widely used to study the electronic properties of graphene, a two-dimensional sheet of carbon atoms [4, 5]. Despite this, the field of electronic transport in graphene has remained very actively debated.

So far, the NEGF method has been mostly used to simulate relatively small systems, due to the cubic scaling of the computational effort associated with matrix inversion. Although an efficient iterative method [6] enables the simulation of very long systems, this method is still restricted to studying quasi-one-dimensional (1D) systems, such as carbon nanotubes and graphene nanoribbons (GNRs). The application of the NEGF method to realistically sized two-dimensional (2D) graphene is still not feasible.

In contrast, for the Kubo-Greenwood method, a real-space linear-scaling method has been developed [7–10] and used to study transport properties of both quasi-1D systems [11–13] and 2D graphene sheets [14–21]. Moreover, this method has

been generalized to studying thermal conductivity [22]. Besides the real-space Kubo method [7–10], which expresses the conductivity as a time-derivative of the mean square displacement, another seemingly different approach [23], which expresses the conductivity as a time-integration of the velocity auto-correlation function, has also been used to study the electronic transport properties of large-scale single-layer [23] and multi-layer [24] graphene sheets, and disordered graphene antidot lattices [25].

Although both of the above methods are based on the Kubo-Greenwood formula, no connection has been made between them. One of our purposes is to identify the time-derivative approach and the time-integration approach as an Einstein relation and the corresponding Green-Kubo relation, and demonstrate their equivalence numerically. Furthermore, a thorough validation of Kubo-Greenwood formula based quantum transport methods for all the transport regimes is also absent. We thus aim to perform a comprehensive evaluation of the applicability of the linear-scaling Kubo-Greenwood quantum transport simulation method for all three transport regimes: the ballistic, diffusive, and localized regimes.

To achieve the above, we find that an efficient implementation is very desirable. Despite the linear-scaling nature of these numerical methods, they are still computationally demanding in most cases. Nowadays, the use of graphics processing units (GPUs) have played a more and more important role in computational physics; finding the solutions to many problems in computational physics has become impressively accelerated by

*Corresponding author

Email address: zheyong.fan@aalto.fi (Zheyong Fan)

using a single or multiple GPUs [26]. In this work, we consider the implementation of the Kubo-Greenwood quantum transport simulation on the GPU, with a unified treatment of the various involved theoretical formalisms and numerical techniques. We will evaluate the performance and correctness of our implementation, as well as the applicability of the method itself.

This paper is organized as follows. In section 2, we present the theoretical background of the Kubo-Greenwood formula and the Green-Kubo and Einstein relations which are both derived. In section 3, we give a detailed discussion of the involved numerical techniques and their GPU implementations. After making a performance evaluation in section 4, we thoroughly evaluate the computational method in different transport regimes in section 5. Section 6 concludes.

2. Theoretical formalism

The Kubo-Greenwood formula [3] for DC conductivity $\sigma_{\mu\nu}^{\text{KG}}(E)$ as a function of the energy E at zero temperature is

$$\sigma_{\mu\nu}^{\text{KG}}(E) = \frac{2\pi\hbar e^2}{\Omega} \text{Tr} [V_\mu \delta(E-H) V_\nu \delta(E-H)]. \quad (1)$$

where \hbar is the reduced Plank constant, e is the electron charge, Ω is the system volume, V_μ is the velocity operator in the μ -direction, H is the Hamiltonian of the system, and Tr denotes the trace. The factor of two results from spin degeneracy. For simplicity, we only consider transport along one direction. Then, the above formula can be simplified to be

$$\sigma^{\text{KG}}(E) = \frac{2\pi\hbar e^2}{\Omega} \text{Tr} [V\delta(E-H)V\delta(E-H)]. \quad (2)$$

By Fourier transforming one of the δ functions in the above formula,

$$\delta(E-H) = \frac{1}{2\pi\hbar} \int_{-\infty}^{+\infty} dt e^{i(E-H)t/\hbar}, \quad (3)$$

we have

$$\sigma(E) = \frac{e^2}{\Omega} \int_{-\infty}^{+\infty} dt \text{Tr} [e^{iEt/\hbar} V e^{-iHt/\hbar} V \delta(E-H)], \quad (4)$$

or equivalently,

$$\sigma(E) = \frac{e^2}{\Omega} \int_{-\infty}^{+\infty} dt \text{Tr} [e^{iHt/\hbar} V e^{-iHt/\hbar} V \delta(E-H)]. \quad (5)$$

due to the remaining δ function. Through a change of variables, $t \rightarrow -t$, we get the following Green-Kubo formula [2, 27], which expresses the running electrical conductivity (REC) as a time-integration of the velocity auto-correlation (VAC) $C_{vv}(E, t)$,

$$\sigma^{\text{GK}}(E, t) = e^2 \rho(E) \int_0^t C_{vv}(E, t) dt, \quad (6)$$

$$C_{vv}(E, t) = \frac{\text{Tr} \left[\frac{2}{\Omega} \delta(E-H) (V(t)V + VV(t)) / 2 \right]}{\text{Tr} \left[\frac{2}{\Omega} \delta(E-H) \right]}, \quad (7)$$

$$\rho(E) = \text{Tr} \left[\frac{2}{\Omega} \delta(E-H) \right], \quad (8)$$

where $V(t) = U^\dagger(t) V U(t) = e^{iHt/\hbar} V e^{-iHt/\hbar}$ is the velocity operator in the Heisenberg representation, and $\rho(E)$ the density of states (DOS). The Green-Kubo relation constitutes essentially the formalism used by Yuan *et al.* [23, 24].

For a specific Green-Kubo formula, there is generally a corresponding Einstein formula. By integrating the Green-Kubo formula, we obtain the following Einstein formula, which expresses the REC as a time-derivative of the mean square displacement (MSD) $\Delta X^2(E, t)$,

$$\sigma^{\text{E1}}(E, t) = e^2 \rho(E) \frac{d}{dt} \Delta X^2(E, t), \quad (9)$$

$$\Delta X^2(E, t) = \frac{\text{Tr} \left[\frac{2}{\Omega} \delta(E-H) (X(t) - X)^2 \right]}{\text{Tr} \left[\frac{2}{\Omega} \delta(E-H) \right]}, \quad (10)$$

where $X(t) = U^\dagger(t) X U(t)$ is the position operator in the Heisenberg representation. An alternative definition, in which the derivative in the above equation is replaced by a division,

$$\sigma^{\text{E2}}(E, t) = e^2 \rho(E) \frac{\Delta X^2(E, t)}{2t}, \quad (11)$$

is frequently used, since it gives smoother curves for the REC than $\sigma^{\text{E1}}(E, t)$ does. The above Einstein relation is exactly the real-space Kubo method [7–10].

We will demonstrate the equivalence of the Green-Kubo formalism and the Einstein formalism numerically. Specifically, we will show that $\sigma^{\text{E1}}(E, t)$ and $\sigma^{\text{GK}}(E, t)$ are equivalent, while $\sigma^{\text{E2}}(E, t)$ deviates from the other two to some degree.

By going from the Kubo-Greenwood formalism to the Green-Kubo or the Einstein formalism, the conductivity becomes a function of not only the energy E , but also the correlation time t . Usually, one takes the following large time limit:

$$\sigma^{\text{KG}}(E) = \lim_{t \rightarrow \infty} \sigma^{\text{GK}}(E, t) = \lim_{t \rightarrow \infty} \sigma^{\text{E1}}(E, t). \quad (12)$$

However, the convergence of this limit is only ensured for diffusive transport, in which case the VAC decays to zero and the MSD becomes proportional to t , resulting in a converged REC. For ballistic transport, the VAC oscillates around a fixed value and the MSD increases quadratically with increasing t , resulting in a divergent REC. In the localized regime, the VAC develops negative values and the slope of the MSD decreases, resulting in a decaying REC.

In this paper, we take graphene as our test system. We use N_x to represent the number of dimer lines located along the zigzag edge and N_y to represent the number of zigzag-shaped chains across the armchair edge. Thus, an $N_x \times N_y$ graphene sample has $N = N_x N_y$ carbon atoms, and the lengths in the zigzag and armchair directions are $L_x = \sqrt{3} N_x a / 2$ and $L_y = 3 N_y a / 2$, respectively, where $a = 0.142$ nm is the carbon-carbon bond length used. For 2D graphene, periodic boundary conditions are applied in both directions; for quasi-1D armchair graphene nanoribbon (AGNR) and zigzag graphene nanoribbon (ZGNR),

we use periodic boundary conditions along the transport (longitudinal) direction, and non-periodic boundary conditions along the perpendicular direction.

We use a nearest-neighbor p_z orbit tight-binding Hamiltonian for pristine systems:

$$H = \sum_{\langle mn \rangle} H_{mn} |m\rangle \langle n| = - \sum_{\langle mn \rangle} \gamma_0 |m\rangle \langle n|, \quad (13)$$

where the hopping parameter γ_0 is chosen to be 2.7 eV. With this notation, the position and velocity operators can be expressed as

$$X = \sum_m X_m |m\rangle \langle m|, \quad (14)$$

$$V = \frac{i}{\hbar} [H, X] = \frac{i}{\hbar} \sum_{\langle mn \rangle} (X_n - X_m) H_{mn} |m\rangle \langle n|. \quad (15)$$

We also consider systems with random single vacancies, which are modeled by removing carbon atoms randomly according to the prescribed defect concentrations. The defect concentration n is determined by the system size N and the number of vacancies N_v as $n = N_v/N$.

3. Numerical implementation

3.1. Numerical approximations

Based on the discussion of the last section, we see that the quantities that need to be calculated are $\rho(E)$, $\rho(E)C_{vv}(E, t)$, and $\rho(E)\Delta X^2(E, t)$. To facilitate the numerical calculation, we firstly rewrite $\rho(E)C_{vv}(E, t)$ and $\rho(E)\Delta X^2(E, t)$ in the following symmetric forms (using the cyclic properties of the trace):

$$\rho(E)C_{vv}(E, t) = \frac{2}{\Omega} \text{Re} \left[\text{Tr} \left[U(t) V \delta(E - H) U(t)^\dagger V \right] \right] \quad (16)$$

$$\rho(E)\Delta X^2(E, t) = \frac{2}{\Omega} \text{Tr} \left[[X, U(t)]^\dagger \delta(E - H) [X, U(t)] \right]. \quad (17)$$

The reason for this will be apparent when we consider the GPU-implementation. To achieve linear-scaling, we have to make three approximations presented below.

3.1.1. Approximation of the trace

The first approximation is to use a random vector $|\phi\rangle$ to evaluate the trace [28]:

$$\text{Tr}[A] \approx \langle \phi | A | \phi \rangle, \quad (18)$$

where A is an arbitrary matrix operator, and $|\phi\rangle$ is normalized to the matrix dimension N , $\langle \phi | \phi \rangle = N$. With this approximation, we have

$$\rho(E) \approx \frac{2}{\Omega} \langle \phi | \delta(E - H) | \phi \rangle, \quad (19)$$

$$\rho(E)C_{vv}(E, t) \approx \frac{2}{\Omega} \text{Re} \left[\langle \phi | U(t) V \delta(E - H) U(t)^\dagger V | \phi \rangle \right], \quad (20)$$

$$\rho(E)\Delta X^2(E, t) \approx \frac{2}{\Omega} \langle \phi | [X, U(t)]^\dagger \delta(E - H) [X, U(t)] | \phi \rangle. \quad (21)$$

The error introduced by this approximation decreases with increasing N . For a given N , the accuracy can also be increased by using a higher number of random vectors. Quantitatively, the relative error is of order $O(1/\sqrt{N_r N})$ [28], where N_r is the number of random vectors.

3.1.2. Approximation of the δ function

The second approximation is related to the δ function. There are various kinds of methods to approximate this, including the Lanczos recursion method (LRM) [29, 30], the Fourier transform method (FTM) [31, 32], and the kernel polynomial method (KPM) [28]. The LRM and the KPM has been compared in Ref. [28]. In this work, we use the FTM and the KPM and give a comparison of them.

In the FTM [31, 32], the δ function is approximated by a truncated discrete Fourier series expansion, and we can rewrite Eqs. (19-21) as

$$\rho(E) \approx \frac{\Delta\tau}{\pi\hbar\Omega} \sum_{n=-N_m}^{+N_m} w_n e^{iEn\Delta\tau/\hbar} F_n^{\text{DOS}}, \quad (22)$$

$$\rho(E)C_{vv}(E, t) \approx \frac{\Delta\tau}{\pi\hbar\Omega} \sum_{n=-N_m}^{+N_m} w_n \text{Re} \left[e^{iEn\Delta\tau/\hbar} F_n^{\text{VAC}}(t) \right], \quad (23)$$

$$\rho(E)\Delta X^2(E, t) \approx \frac{\Delta\tau}{\pi\hbar\Omega} \sum_{n=-N_m}^{+N_m} w_n e^{iEn\Delta\tau/\hbar} F_n^{\text{MSD}}(t), \quad (24)$$

where F_n^{DOS} , $F_n^{\text{VAC}}(t)$, and $F_n^{\text{MSD}}(t)$ are the Fourier moments:

$$F_n^{\text{DOS}} \approx \langle \phi | U(n\Delta\tau) | \phi \rangle, \quad (25)$$

$$F_n^{\text{VAC}}(t) \approx \langle \phi | U(t) V U(n\Delta\tau) U(t)^\dagger V | \phi \rangle, \quad (26)$$

$$F_n^{\text{MSD}}(t) \approx \langle \phi | [X, U(t)]^\dagger U(n\Delta\tau) [X, U(t)] | \phi \rangle. \quad (27)$$

Note that a window function should be applied before performing the Fourier transform to suppress the unwanted Gibbs oscillation. Usually, a Hanning window

$$w_n = \frac{1}{2} \left[1 + \cos \left(\frac{\pi n}{N_m + 1} \right) \right] \quad (28)$$

is used [31]. We will discuss the choice of the time step $\Delta\tau$ used in the above Fourier transforms when we compare the relative performance of the FTM and the KPM in the next section.

In the KPM [28], the δ function is approximated by a truncated Chebyshev polynomial expansion, and we can rewrite Eqs. (19-21) as

$$\rho(E) \approx \frac{2}{\pi\Omega\sqrt{1-E^2}} \sum_{n=0}^{N_m-1} g_n (2 - \delta_{n0}) T_n(E) C_n^{\text{DOS}}, \quad (29)$$

$$\rho(E)C_{vv}(E, t) \approx \frac{2}{\pi\Omega\sqrt{1-E^2}} \sum_{n=0}^{N_m-1} g_n (2 - \delta_{n0}) \text{Re} \left[T_n(E) C_n^{\text{VAC}}(t) \right], \quad (30)$$

$$\rho(E)\Delta X^2(E, t) \approx \frac{2}{\pi\Omega\sqrt{1-E^2}} \sum_{n=0}^{N_m-1} g_n (2 - \delta_{n0}) T_n(E) C_n^{\text{MSD}}(t), \quad (31)$$

where $T_n(E)$ is the n th order Chebyshev polynomial of the first kind and C_n^{DOS} , $C_n^{\text{VAC}}(t)$, and $C_n^{\text{MSD}}(t)$ are the Chebyshev moments:

$$C_n^{\text{DOS}} \approx \langle \phi | T_n(H) | \phi \rangle, \quad (32)$$

$$C_n^{\text{VAC}}(t) \approx \langle \phi | U(t) V T_n(H) U(t)^\dagger V | \phi \rangle, \quad (33)$$

$$C_n^{\text{MSD}}(t) \approx \langle \phi | [X, U(t)]^\dagger T_n(H) [X, U(t)] | \phi \rangle. \quad (34)$$

Similarly, a damping factor should be applied before performing the Chebyshev summation in order to suppress the Gibbs oscillation. Usually, the Jackson damping [28]

$$g_n = (1 - n\alpha) \cos(\pi n\alpha) + \alpha \sin(\pi n\alpha) \cot(\pi\alpha), \quad (35)$$

where $\alpha = 1/(N_m + 1)$ is used. Note that the above Chebyshev expansions assume that H has been scaled and shifted [28] so that the spectrum lies in the interval $[-1, 1]$.

Both the Fourier and the Chebyshev moments can be evaluated iteratively. Detailed algorithms will be presented when we consider the GPU-implementation.

3.1.3. Approximation of the time-evolution

The third approximation is to evaluate the application of the time-evolution operators on state vectors using a finite-term polynomial expansion. From the discussion above, we see that there are three kinds of time-evolution operators: $U(\Delta t)$, $U(\Delta t)^\dagger = U(-\Delta t)$, and $[X, U(t)]$. Their operations can be evaluated very accurately and efficiently in a linear-scaling way by using the Chebyshev polynomial expansion [33, 34]:

$$U(\pm\Delta t) \approx \sum_{m=0}^{N_p-1} (2 - \delta_{0m})(\mp i)^m J_m\left(\frac{\Delta t}{\hbar}\right) T_m(H), \quad (36)$$

$$[X, U(\Delta t)] \approx \sum_{m=0}^{N_p-1} (2 - \delta_{0m})(-i)^m J_m\left(\frac{\Delta t}{\hbar}\right) [X, T_m(H)], \quad (37)$$

where $J_m\left(\frac{\Delta t}{\hbar}\right)$ is the m th order Bessel function of the first kind. Time-evolution of quantum states has also been considered with regard to GPU computation in other contexts [35–37]. The above expansions assume that the spectrum of H lies in the interval $[-1, 1]$. For a Hamiltonian with spectrum beyond this range, we need to shift and scale it, with a corresponding opposite scaling of the time interval Δt . The order of expansion N_p depends on the time interval Δt and the desired accuracy. The above summations can be efficiently evaluated by using the following recursion relations ($m \geq 2$):

$$T_m(H) = 2HT_{m-1}(H) - T_{m-2}(H), \quad (38)$$

$$[X, T_m(H)] = 2[X, H]T_{m-1}(H) + 2H[X, T_{m-1}(H)] - [X, T_{m-2}(H)], \quad (39)$$

$$T_0(H) = 1 \quad T_1(H) = H, \quad (40)$$

$$[X, T_0(H)] = 0, \quad [X, T_1(H)] = [X, H]. \quad (41)$$

3.2. GPU implementation

In this subsection, we consider the GPU implementation of the algorithms. We use CUDA [38] as our developing tool. We only discuss the relevant techniques of our CUDA implementation when appropriate; the reader is referred to the official programming guide [38] for more details.

To achieve high performance, we implement nearly all of the algorithms on the GPU, minimizing data transfer between the

CPU and the GPU. Here we present the pseudo codes for calculating $\rho(E)$, $\rho(E)C_{vv}(E, t)$, and $\rho(E)\Delta X^2(E, t)$ in Algorithms 1, 2, and 3, respectively. While for $\rho(E)$, we only need to calculate one set of moments, for $\rho(E)C_{vv}(E, t)$ and $\rho(E)\Delta X^2(E, t)$, we have to calculate a set of moments at each correlation time t_m ($0 \leq m < N_c$). Thus, calculating the conductivity is generally much more demanding than calculating the DOS. Note that we only calculate the moments in the GPU, and copy their results to the CPU for performing the Fourier transform or the Chebyshev summation. We could do all the calculations in the GPU, but it does not result in a significant gain in the overall performance, since the calculation of the moments takes the majority of the computation time.

In the previous subsection, we have written $\rho(E)C_{vv}(E, t)$ and $\rho(E)\Delta X^2(E, t)$ in symmetric forms. The advantage is that we can use the following iteration relations to calculate the conductivity at different correlation times:

$$U^\dagger(t + \Delta t)V|\phi\rangle = U^\dagger(\Delta t)U^\dagger(t)V|\phi\rangle, \quad (42)$$

$$\langle \phi | U(t + \Delta t)V = \langle \phi | U(t)U(\Delta t)V, \quad (43)$$

$$[X, U(t + \Delta t)]|\phi\rangle = U(\Delta t)[X, U(t)]|\phi\rangle + [X, U(\Delta t)]U(t)|\phi\rangle. \quad (44)$$

Algorithm 1 Pseudo code for calculating $\rho(E)$.

- 1: **if** use the FTM **then**
 - 2: calculate F_n^{DOS} in Eq. (25) in the GPU
 - 3: copy the F_n^{DOS} data from the GPU to the CPU
 - 4: calculate $\rho(E)$ in the CPU using Eq. (22)
 - 5: **end if**
 - 6: **if** use the KPM **then**
 - 7: calculate C_n^{DOS} in Eq. (32) in the GPU
 - 8: copy the C_n^{DOS} data from the GPU to the CPU
 - 9: calculate $\rho(E)$ in the CPU using Eq. (29)
 - 10: **end if**
-

Algorithm 2 Pseudo code for calculating $\rho(E)C_{vv}(E, t)$.

Require: $|\phi\rangle$ is the initial random vector

- 1: **for** $m = 1$ to $N_c - 1$ **do**
 - 2: calculate $U^\dagger(t_m)V|\phi\rangle$ iteratively using Eq. (42)
 - 3: calculate $\langle \phi | U(t_m)V$ iteratively using Eq. (43)
 - 4: **if** use the FTM **then**
 - 5: calculate F_n^{VAC} in Eq. (26) in the GPU
 - 6: copy the F_n^{VAC} data from the GPU to the CPU
 - 7: calculate $\rho(E)C_{vv}(E, t_m)$ in the CPU using Eq. (23)
 - 8: **end if**
 - 9: **if** use the KPM **then**
 - 10: calculate C_n^{VAC} in Eq. (33) in the GPU
 - 11: copy the C_n^{VAC} data from the GPU to the CPU
 - 12: calculate $\rho(E)C_{vv}(E, t_m)$ in the CPU using Eq. (30)
 - 13: **end if**
 - 14: **end for**
-

The calculation of the moments in both the FTM and the KPM used in the above three algorithms can also be carried

Algorithm 3 Pseudo code for calculating $\rho(E)\Delta X^2(E, t)$.

Require: $|\phi\rangle$ is the initial random vector

```

1: for  $m = 0$  to  $N_c - 1$  do
2:   calculate  $[X, U(t_m)]|\phi\rangle$  iteratively using Eq. (44)
3:   if use the FTM then
4:     calculate  $F_n^{\text{MSD}}$  in Eq. (27) in the GPU
5:     copy the  $F_n^{\text{MSD}}$  data from the GPU to the CPU
6:     calculate  $\rho(E)\Delta X^2(E, t_m)$  in the CPU using Eq. (24)
7:   end if
8:   if use the KPM then
9:     calculate  $C_n^{\text{MSD}}$  in Eq. (34) in the GPU
10:    copy the  $C_n^{\text{MSD}}$  data from the GPU to the CPU
11:    calculate  $\rho(E)\Delta X^2(E, t_m)$  in the CPU using Eq. (31)
12:   end if
13: end for

```

out iteratively. We note that the Fourier moments in equations (25 - 27) can be expressed in a unified way:

$$F_n \approx \langle \phi_L | U(n\Delta t) | \phi_R \rangle. \quad (45)$$

Different moments only differ in $|\phi_L\rangle$ and $|\phi_R\rangle$: for DOS, $|\phi_L\rangle = |\phi_R\rangle = |\phi\rangle$; for VAC, $|\phi_L\rangle = VU^\dagger(t)|\phi\rangle$ and $|\phi_R\rangle = U^\dagger(t)V|\phi\rangle$; for MSD, $|\phi_L\rangle = |\phi_R\rangle = [X, U(t)]|\phi\rangle$. Similarly, the Chebyshev moments in equations (32 - 34) can be expressed uniformly as

$$C_n \approx \langle \phi_L | T_n(H) | \phi_R \rangle. \quad (46)$$

Thus, we can present the calculations of these different moments in a unified way, as shown in Algorithms 4 and 5.

Algorithm 4 Pseudo code for calculating the Fourier moments $F_n = \langle \phi_L | U(n\Delta\tau) | \phi_R \rangle$.

```

1: kernel:  $|\phi'_R\rangle \leftarrow |\phi_R\rangle$ 
2: kernel:  $F_0 \leftarrow \langle \phi_L | \phi'_R \rangle$ 
3: for  $n = 1$  to  $N_m$  do
4:   calculate  $|\phi'_R\rangle \leftarrow U(\Delta\tau)|\phi'_R\rangle$  in the GPU
5:   kernel:  $F_n \leftarrow \langle \phi_L | \phi'_R \rangle$ 
6: end for
7: kernel:  $|\phi'_R\rangle \leftarrow |\phi_R\rangle$ 
8: for  $n = 1$  to  $N_m$  do
9:   calculate  $|\phi'_R\rangle \leftarrow U^\dagger(\Delta\tau)|\phi'_R\rangle$  in the GPU
10:  kernel:  $F_{-n} \leftarrow \langle \phi_L | \phi'_R \rangle$ 
11: end for

```

We next consider the time-evolution of quantum states. In Algorithms 6 and 7, we present the algorithms for evaluating $|\phi_{\text{out}}\rangle = U(\pm\Delta t)|\phi_{\text{in}}\rangle$ and $|\phi_{\text{out}}\rangle = [X, U(\Delta t)]|\phi_{\text{in}}\rangle$, according to Eq. (36) and Eq. (37), respectively. In Algorithm 6, besides the input vector $|\phi_{\text{in}}\rangle$, and the output vector $|\phi_{\text{out}}\rangle$, we need three auxiliary vectors, $|\phi_0\rangle$, $|\phi_1\rangle$, and $|\phi_2\rangle$. In Algorithm 7, we need another set of auxiliary vectors, $|\phi_0^x\rangle$, $|\phi_1^x\rangle$, and $|\phi_2^x\rangle$. All of these vectors should be defined in global memory in order to pass data between kernels.

An examination of Algorithms 6 and 7 reveals that, apart from some simple linear transformations, the only nontrivial calculations are the matrix-vector multiplications, $|\phi_{\text{out}}\rangle =$

Algorithm 5 Pseudo code for calculating the Chebyshev moments $C_n = \langle \phi_L | T_n(H) | \phi_R \rangle$.

```

1: kernel:  $|\phi_0\rangle \leftarrow |\phi_R\rangle$ 
2: kernel:  $C_0 \leftarrow \langle \phi_L | \phi_0 \rangle$ 
3: kernel:  $|\phi_1\rangle \leftarrow H|\phi_0\rangle$ 
4: kernel:  $C_1 \leftarrow \langle \phi_L | \phi_1 \rangle$ 
5: for  $n = 2$  to  $N_m - 1$  do
6:   kernel:  $|\phi_2\rangle \leftarrow 2H|\phi_1\rangle - |\phi_0\rangle$ 
7:   kernel:  $C_n \leftarrow \langle \phi_L | \phi_2 \rangle$ 
8: end for

```

Algorithm 6 Pseudo code for calculating $|\phi_{\text{out}}\rangle = U(\pm\Delta t)|\phi_{\text{in}}\rangle$

```

1: kernel:  $|\phi_0\rangle \leftarrow |\phi_{\text{in}}\rangle$ 
2: kernel:  $|\phi_1\rangle \leftarrow H|\phi_0\rangle$ 
3: kernel:  $|\phi_{\text{out}}\rangle \leftarrow J_0\left(\frac{\Delta t}{\hbar}\right)|\phi_0\rangle + 2(\mp i)J_1\left(\frac{\Delta t}{\hbar}\right)|\phi_1\rangle$ 
4: for  $m = 2$  to  $N_p - 1$  do
5:   kernel:  $|\phi_2\rangle \leftarrow 2H|\phi_1\rangle - |\phi_0\rangle$ 
6:   kernel:  $|\phi_{\text{out}}\rangle \leftarrow |\phi_{\text{out}}\rangle + 2(\mp i)^m J_m\left(\frac{\Delta t}{\hbar}\right)|\phi_2\rangle$ 
7:   Permute pointers:  $|\phi_0\rangle \leftarrow |\phi_1\rangle, |\phi_1\rangle \leftarrow |\phi_2\rangle, |\phi_2\rangle \leftarrow |\phi_0\rangle$ 
8: end for

```

Algorithm 7 Pseudo code for calculating $|\phi_{\text{out}}\rangle = [X, U(\Delta t)]|\phi_{\text{in}}\rangle$

```

1: kernel:  $|\phi_0\rangle \leftarrow |\phi_{\text{in}}\rangle$ 
2: kernel:  $|\phi_0^x\rangle \leftarrow 0$ 
3: kernel:  $|\phi_1\rangle \leftarrow H|\phi_0\rangle$ 
4: kernel:  $|\phi_1^x\rangle \leftarrow [X, H]|\phi_{\text{in}}\rangle$ 
5: kernel:  $|\phi_{\text{out}}\rangle \leftarrow 2(-i)J_1\left(\frac{\Delta t}{\hbar}\right)|\phi_1^x\rangle$ 
6: for  $m = 2$  to  $N_p - 1$  do
7:   kernel:  $|\phi_2\rangle \leftarrow 2H|\phi_1\rangle - |\phi_0\rangle$ 
8:   kernel:  $|\phi_2^x\rangle \leftarrow 2[X, H]|\phi_1\rangle + 2H|\phi_1^x\rangle - |\phi_0^x\rangle$ 
9:   kernel:  $|\phi_{\text{out}}\rangle \leftarrow |\phi_{\text{out}}\rangle + 2(-i)^m J_m\left(\frac{\Delta t}{\hbar}\right)|\phi_2^x\rangle$ 
10:  Permute pointers:  $|\phi_0\rangle \leftarrow |\phi_1\rangle, |\phi_1\rangle \leftarrow |\phi_2\rangle, |\phi_2\rangle \leftarrow |\phi_0\rangle$ 
11:  Permute pointers:  $|\phi_0^x\rangle \leftarrow |\phi_1^x\rangle, |\phi_1^x\rangle \leftarrow |\phi_2^x\rangle, |\phi_2^x\rangle \leftarrow |\phi_0^x\rangle$ 
12: end for

```

$H|\phi_{\text{in}}\rangle$ and $|\phi_{\text{out}}\rangle = [X, H]|\phi_{\text{in}}\rangle$. In Algorithm 8, we present the pseudo code of the CUDA kernel which evaluates $|\phi_{\text{out}}\rangle = H|\phi_{\text{in}}\rangle$; the evaluation of $|\phi_{\text{out}}\rangle = [X, H]|\phi_{\text{in}}\rangle$ is very similar.

The strategy in Algorithm 8 is to use one thread for one element of the output vector. By using a block size of S_b , the number of blocks in the kernel is $(N - 1)/S_b + 1$, where N is the number of sites in the system. Thus, this kernel is executed with the configuration of $\langle\langle\langle (N - 1)/S_b + 1, S_b \rangle\rangle\rangle$. The **if** statement on line 1 is necessary to avoid manipulating invalid memory in the case of N not being an integer multiple of S_b . Lines 2-7 are devoted to the calculation of $\phi_{\text{out}}[n]$, where the variable *temp* is used to reduce the global memory access, which is very time-consuming. We use a neighbor list to specify the Hamiltonian, denoting the number of neighbors to site n as NN_n , and indexing the k th neighbor of site n as NL_{nk} . For a sparse Hamiltonian, NN_n is much smaller than the total number of sites N . The NL_{nk} data should be coded in such a way that the indices of the k th neighbor sites for all the sites are stored consecutively, i.e., in the order of $\text{NL}_{00}, \text{NL}_{10}, \text{NL}_{20}, \dots, \text{NL}_{01}, \text{NL}_{11}, \text{NL}_{21}, \dots, \text{NL}_{0k}, \text{NL}_{1k}, \text{NL}_{2k}, \dots$. This special order ensures coalescing in global memory access, which means that consecutive threads access consecutive data in the global memory. This requirement has also been noticed in our previous work on molecular dynamics simulations [39].

Algorithm 8 The algorithm for evaluating $|\phi_{\text{out}}\rangle = H|\phi_{\text{in}}\rangle$

Require: $\phi_{\text{in}}[m]$ is the m th component of $|\phi_{\text{in}}\rangle$
Require: $\phi_{\text{out}}[n]$ is the n th component of $|\phi_{\text{out}}\rangle$
Require: $n = \text{blockIdx.x} * \text{blockDim.x} + \text{threadIdx.x}$
Require: N is the number of sites in the system
Require: NN_n is the total number of neighbor sites of site n
Require: NL_{nk} is the index of the k th neighbor site of site n

- 1: **if** $n < N$ **then**
- 2: $\text{temp} \leftarrow 0$
- 3: **for** $k = 0$ to $\text{NN}_n - 1$ **do**
- 4: $m \leftarrow \text{NL}_{nk}$
- 5: $\text{temp} \leftarrow \text{temp} + H_{nm}\phi_{\text{in}}[m]$
- 6: **end for**
- 7: $\phi_{\text{out}}[n] \leftarrow \text{temp}$
- 8: **end if**

4. Performance evaluation

In this section, we compare the relative performance of our GPU and CPU implementations, and the relative performance of the FTM and the KPM.

4.1. GPU versus CPU

We firstly evaluate the relative performance of our GPU implementation with respect to our CPU implementation. The comparison is made between a Tesla K20 GPU card and an Intel Xeon E5-1620 @ 3.60 GHz CPU core. The serial CPU code is implemented in C/C++ and is compiled with an O3 optimization mode. Although the algorithms in the previous section are presented by using a complex number notation, in both

the CPU and the GPU implementation, we use two real vectors for a complex state vector, which can save nearly half of the calculations compared with a naive use of the intrinsic complex number. Both the CPU and the GPU code use double-precision arithmetics.

The major computation which scales linearly with the system size is the Chebyshev iteration, which is used for both the time-evolution and the KPM. We thus present a performance evaluation of the Chebyshev iteration part of the code in some detail. We chose to present the testing results for $|\phi_2\rangle = 2H|\phi_1\rangle - |\phi_0\rangle$; those for $|\phi_2^x\rangle = 2[X, H]|\phi_1\rangle + 2H|\phi_1^x\rangle - |\phi_0^x\rangle$ are similar.

Figure 1 shows the results of the performance evaluation of the Chebyshev iteration part, where the speedup factor is defined as the computation time in the CPU over that in the GPU. The computational time in the CPU scales linearly with respect to the simulation size, which reflects the linear-scaling nature of the algorithm. The computation time in the GPU also scales linearly approximately. The speedup factor increases from about 10.5 to about 16.5 with the number of atoms in the simulated system increasing from 0.2 million to 1.6 million and nearly saturates thereafter. For all the other calculations such as the evaluation of the inner products, we also obtained a comparable speedup factor. The overall speedup factor of our GPU implementation over our CPU implementation is observed to be about 16.

This speedup factor seems to be not very impressive. Indeed, in our recent work on exact diagonalization of the Hubbard model using the LRM on the GPU [40], a speedup factor of about 60 is obtained using double-precision. The difference in the speedup factor results from the different computational intensities of the problems. For example, in the Hubbard model, for a Hamiltonian size of 853776 (12 spin sites), the computation times for one Lanczos iteration in the CPU and the GPU are about 120 ms and 2 ms, respectively, giving a speedup factor of 60 [40]. In comparison, for our tight-binding model with a Hamiltonian size of 10^6 , the computation times for one Chebyshev iteration in the CPU and the GPU are about 12.8 ms and 0.8 ms, giving a speedup factor of 16. We see that for a given Hamiltonian size, the Hubbard model is about 10 times more computationally intensive than the single-particle tight-binding model and attains a higher speedup factor. Similar dependence of the speedup factor on the computational intensity has also been observed in our recent work on molecular dynamics simulation [39].

4.2. KPM versus FTM

We then give a comparison of the relative performance of the KPM and the FTM. For the FTM, the calculation of each Fourier moment involves a time-evolution with a time step $\Delta\tau$. The choice of the time step used in the FTM is related to the Nyquist sampling rates used in digital signal analysis: it should not be too large to give aliasing errors, and not too small to reduce the energy resolution [31]. The optimal value of $\Delta\tau$ corresponding to a maximum bandwidth ΔE of the energy spectrum without aliasing error can be fixed to be

$$\Delta\tau = \frac{2\pi\hbar}{\Delta E}. \quad (47)$$

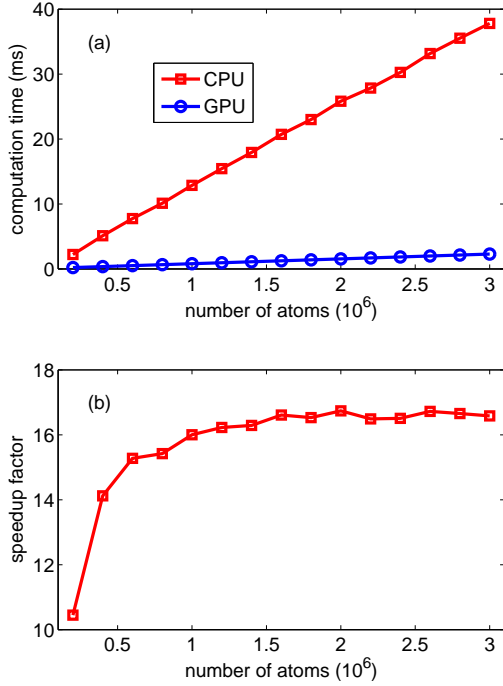


Figure 1: (Color online) (a) Computation times for evaluating $|\phi_2\rangle = 2H|\phi_1\rangle - |\phi_0\rangle$ in the CPU and the GPU and (b) the corresponding speedup factor as a function of the system size. Double-precision is used for both the CPU and the GPU code.

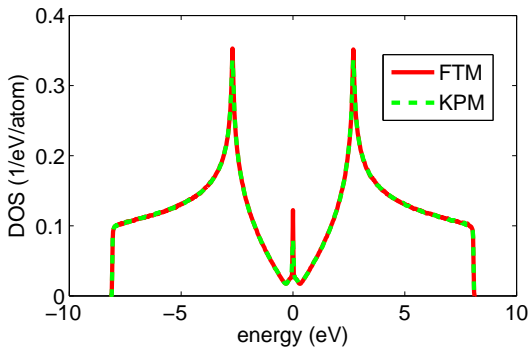


Figure 2: (Color online) DOS as a function of energy for 2D graphene of size 2048×1024 (using 10 random vectors) with defect density $n = 1\%$ calculated by the KPM with $N_m = 1000$ and the FTM with $2N_m + 1 = 1001$.

For a scaled Hamiltonian with spectrum $[-1, 1]$, we have $\Delta E = 2$ and $\Delta\tau = \pi\hbar$. Then, the dimensionless argument in the Bessel function is π , which determines the number of Chebyshev iterations in the time evolution operator $U(\Delta\tau)$ to be about $N_p = 20$ for an accuracy of 10^{-15} . In contrast, the calculation of each Chebyshev moment in the KPM only involves one Chebyshev iteration.

To give a fair comparison of the relative efficiency, we should also consider the energy resolution δE , which is related to the number of moments $2N_m + 1$ in the FTM and N_m in the KPM. Quantitatively, we have

$$\delta E = \frac{2\pi\hbar}{\Delta\tau(2N_m + 1)} = \frac{\Delta E}{2N_m + 1} \quad (48)$$

in the FTM [31] and

$$\delta E = \frac{\pi\Delta E}{N_m} \quad (49)$$

in the KPM [28], respectively. Figure 2 gives a comparison of the DOSs calculated by the the KPM with $N_m = 1000$ and the FTM with $2N_m + 1 = 1001$. We see that they give consistent results and the FTM indeed has a higher energy resolution when using the same number of moments.

By combining the above analysis, we come to the conclusion that the KPM is about $20/\pi \approx 6.4$ times as efficient as the FTM for achieving the same energy resolution. However, for the transport simulations, this difference of efficiency only matters in the diffusive regime, where the correlation time step Δt should be relatively small, and the computation time is dominated by the calculation of the δ function. In the localized regime, where the correlation time step is usually chosen to be very large, the computation time is dominated by the time-evolution $[X, U(t)]|\phi\rangle$, and the relative efficiency of the KPM over the FTM does not lead to a significant gain in performance for the whole simulation.

5. Validation

In this section, we validate our GPU code by studying the transport properties of 2D graphene and quasi-1D graphene nanoribbons in both the ballistic, the diffusive and the localized regimes.

5.1. The ballistic transport regime

For ballistic transport without any scattering, the VAC does not decay with time, resulting in a divergent conductivity. A finite conductance can only be deduced by introducing a length scale. While there is no intrinsic definition of length in the Green-Kubo and the Einstein formulas, a definition of length in terms of the MSD,

$$L(E, t) = 2\sqrt{\Delta X^2(E, t)} \quad (50)$$

is frequently used [10, 17, 18]. The conductance of a system with width W can be defined as

$$G(E) = \frac{W}{L(E, t)}\sigma^{\text{E1}}(E, t). \quad (51)$$

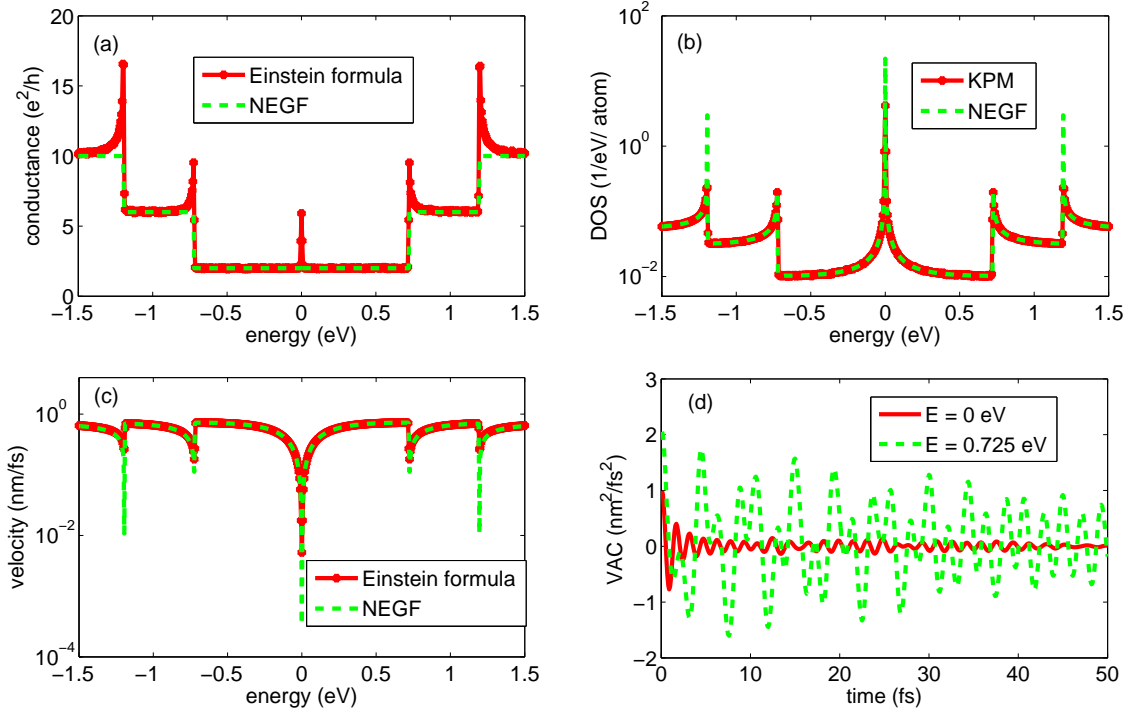


Figure 4: (Color online) Ballistic transport properties for pristine ZGNR of size 65536×16 (using 100 random vectors). (a) Ballistic conductance as a function of energy calculated by the Einstein formula (Eq. (51)) and the NEGF method. (b) DOS calculated by the KPM and the NEGF method. (c) $\sqrt{v^2(E)}$ as a function of energy deduced from the calculated DOS and conductance by using Eq. (52). (d) VACs as a function of correlation time for the Dirac point and the next band edge.

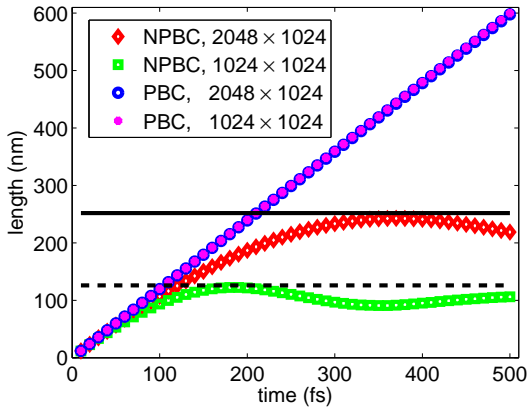


Figure 3: (Color online) Length defined by $L = 2\sqrt{\Delta X^2(E, t)}$ as a function of the correlation time for pristine graphene with different sizes and different boundary conditions along the transport direction (the zigzag direction): periodic (PBC) and non-periodic (NPBC). The solid and dashed horizontal lines indicate the sample lengths along the transport direction: 126 nm and 252 nm for 1024×1024 graphene and 2048×1024 graphene, respectively.

Although the correlation time t appears in the above equation, a converged time-independent (length-independent) value of $G(E)$ can be obtained within a short correlation time. We note that the factor of 2 in the above length definition is necessary to obtain correct results if we use the correct definition of conductivity, $\sigma^{E1}(E, t)$, rather than the alternative, $\sigma^{E2}(E, t)$, which is half of $\sigma^{E1}(E, t)$ in the ballistic regime.

To justify the factor of 2 in Eq. (50), we examine the time-dependence of the length for pristine graphene with different sizes and different boundary conditions along the transport direction, which is chosen to be the zigzag direction. By applying periodic boundary conditions in the transport direction, there is no noticeable difference in the results obtained by using a longer sample (252 nm for 2048×1024 graphene) and a shorter sample (126 nm for 1024×1024 graphene), which reflects the small finite size effect in Green-Kubo-like formulas [39]. In contrast, by imposing a non-periodic boundary condition in the transport direction, the diffusion of electrons is confined by the sample size, with the maximum diffusion length as defined in Eq. (50) being the length of the sample. The factor of 2 can also be understood intuitively: $\sqrt{\Delta X^2(E, t)}$ is the absolute diffusion distance in one direction, and the factor of 2 accounts for the diffusion in the opposite direction.

We now study the ballistic transport properties of a 65536×16 pure ZGNR by comparing the results with those obtained by the NEGF method. As can be seen from Fig. 4 (a), the overall plateaus of the quantized conductance can be correctly pro-

duced by Eq. (51), but the conductances around the band edges are overestimated. Markussen *et al.* [12] also noticed this problem and argued that the overshoots near the band edges originate from the nonequivalence between the expectation values of $v(E)$ and the square root of the expectation value of $v^2(E)$. Here, we give an analysis of this problem from the numerical perspective.

In the ballistic regime, the VAC oscillates around some value (see Fig. 4 (d) for an example), and an average value of $v^2(E)$ can be well established over a short correlation time. Thus we can express the MSD as $\Delta X^2(E, t) = v^2(E)t^2$, which results in the following expression for the conductance:

$$G(E) = \frac{W}{2} e^2 \rho(E) \sqrt{v^2(E)}. \quad (52)$$

Fig. 4 (b) presents the calculated DOS and Fig. 4 (c) presents the deduced $\sqrt{v^2(E)}$. We see that both $\rho(E)$ and $\sqrt{v^2(E)}$ are singular near the band edges. Thus, the calculation of ballistic conductance in the Einstein formalism involves multiplications of big and small numbers, which is numerically unstable. Since the MSD and the VAC are squared quantities, we obtain an overestimation rather than an underestimation of the conductance.

5.2. The diffusive transport regime

We now turn to discuss the diffusive transport regime. We consider 2D graphene of size 2048×1024 with defect concentration $n = 1\%$. We use both the Green-Kubo formula and the Einstein formula. The time step is chosen to be $\Delta t = 0.1$ fs, small enough to exhibit the detailed features of the ballistic-to-diffusive transition.

Figure 5 (a-c) shows the VACs for different energies as a function of correlation time. We see that the VAC does not decay monotonically. For the Dirac point $E = 0.0$ eV, the VAC decays to zero within one fs and then develops negative values up to 5 fs, after which the VAC stays at zero for a relatively long time. For higher energies, $E = 0.5$ eV and 1.0 eV, apart from the expected exponential decay, there is also an oscillatory component. This oscillation has been discussed by de Laissardiere *et al.* [16], and is attributed to the Zitterbewegung effect. A spectral analysis shows that the frequency ω of the oscillation is directly related to the electron energy by $\omega = 2E/\hbar$, which is consistent with the oscillation factor $\cos^2(Et/\hbar)$ in the VAC [16]. By going from the Green-Kubo to the Einstein formalism, these oscillations are smoothed out, as shown by the MSD curves in Figure 5 (d-f). The ballistic-to-diffusive transition is featured by the decay of the VAC in the Green-Kubo formalism, or the quadratic-to-linear transition of the MSD in the Einstein formalism.

From the VAC and the MSD, we can calculate RECs, $\sigma^{\text{GK}}(E, t)$, $\sigma^{\text{E1}}(E, t)$, and $\sigma^{\text{E2}}(E, t)$, as shown in Fig. 5 (g-i). We see that the derivative-based definition of the REC in the Einstein formalism is equivalent to the REC defined in the Green-Kubo formalism: $\sigma^{\text{E1}}(E, t) = \sigma^{\text{GK}}(E, t)$. In contrast, the division-based definition of the REC in the Einstein formalism deviates from the other two in the ballistic-to-diffusive regime.

One may note that for the Dirac point, $\sigma^{\text{E1}}(E, t)$ has large fluctuations when $t > 10$ fs. This reflects the numerical difficulty of calculating the derivative in Eq. (9), especially for small time steps, and is probably the reason for the preference of using $\sigma^{\text{E2}}(E, t)$ instead of $\sigma^{\text{E1}}(E, t)$ in some previous works. However, we stress that $\sigma^{\text{E2}}(E, t)$ is a wrong definition in principle and should be used with caution.

The most interesting quantity in the diffusive regime is the semi-classical conductivity, σ_{sc} , which is conventionally defined [11–21] to be the maximum value of the REC:

$$\sigma_{\text{sc}}(E) = \max\{\sigma(E, t), t > 0\}. \quad (53)$$

Using this definition, the calculated $\sigma_{\text{sc}}(E)$ (the solid line in Fig. 6) exhibits a plateau of minimum conductivity $\sigma_{\text{min}} = 4e^2/(\pi h)$ in the range of $|E| < 0.25$ eV, along with a peak around the Dirac point. Similar results have been obtained by Yuan *et al.* using the Green-Kubo formula [23] and by Cresti *et al.* using the Einstein formula [21]. One may note that the peaks found by Yuan *et al.* [23] are much lower than those found by Cresti *et al.* [21]. This difference partly results from the different numerical approaches, but the major reason is that Cresti *et al.* use Eq. (53) to calculate $\sigma_{\text{sc}}(E)$, while Yuan *et al.* just integrate the VAC to some given correlation time.

A comment on the connection and difference between the Green-Kubo method in our work and the numerical approach developed by Yuan *et al.* is in order. After some algebra, we can rewrite their formula for DC conductivity (Eq. (41) in Ref. [23]) using our notations as:

$$\sigma(E, t) \approx \frac{2e^2}{\Omega} \int_0^t \text{Re} \left[\langle \phi | V U^\dagger(t) V U(t) | \delta(E - H) | \phi \rangle \right], \quad (54)$$

which is equivalent to Eq. (6) and Eq. (20) in our work. The difference between our approach and theirs is mainly related to the numerical implementations. They firstly precompute all the “quasi-eigenstates” $|E_m\rangle = \delta(E_m - H)|\phi\rangle \approx \frac{\Delta\tau}{2\pi\hbar} \sum_{n=-N_m}^{+N_m} e^{iE_m n \Delta\tau/\hbar} U(n\Delta\tau)|\phi\rangle$ for a given number of energy points E_m and then store them in memory, before calculating $\sigma(E, t)$ using Eq. (54). This strategy may be very efficient, but is not economic in terms of memory usage, restricting the number of energy points considered in one simulation to be around 64 [24].

Although Eq. (53) has been widely used, there is no rigorous justification for using it. The reason for choosing this definition may be related to the unavoidable localization effects [16–21] in most of the problems studied by this method. When localization takes place, the REC decays with increasing correlation time after achieving the diffusive regime, and it is difficult to apply Eq. (12) to find a time-independent (length-independent) $\sigma_{\text{sc}}(E)$. Although Eq. (53) works fine for higher energies, it is problematic near the Dirac point. From Fig. 5 (g) we see that, the correctly defined REC drops abruptly from 1 fs to 5 fs and much more slowly when $t > 10$ fs. While the latter slow decay is a sign of weak localization, which is usually a precursor of strong localization, the earlier fast decay cannot be attributed to a localization effect. Thus, the peak value around 1 fs (corresponding to a length of about 1 nm) cannot be taken as the

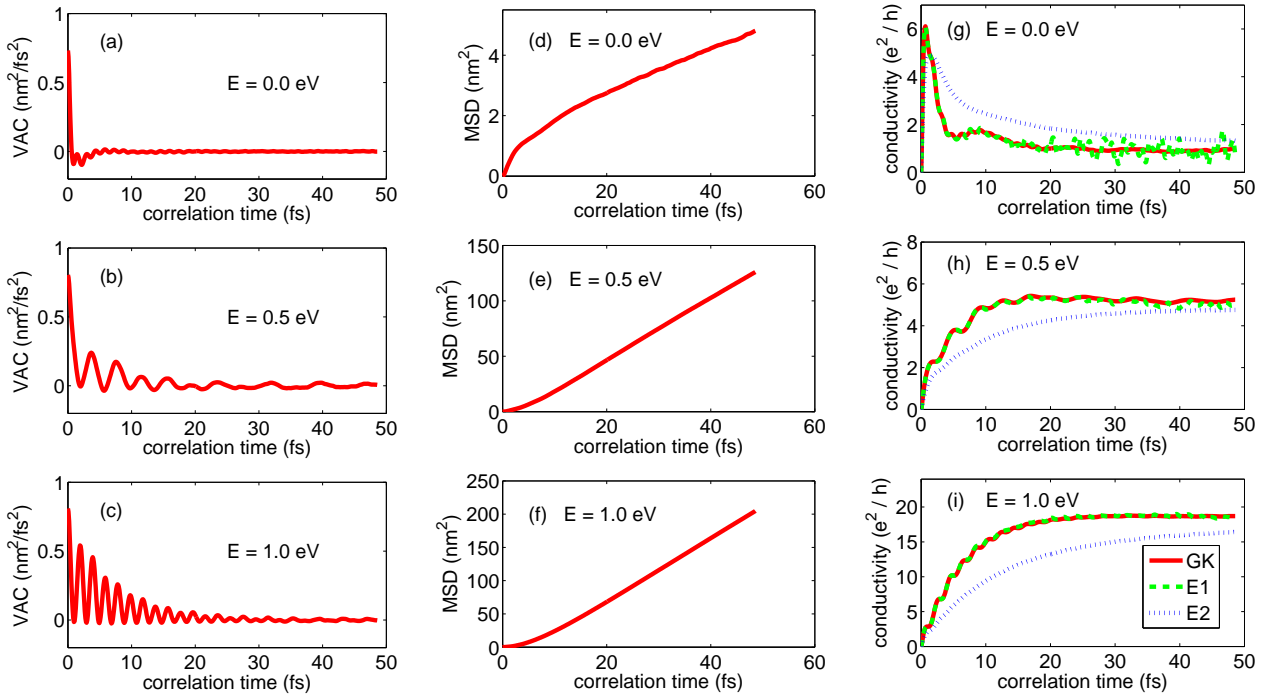


Figure 5: (Color online) (a-c) VACs, (d-f) MSDs, and (g-i) RECs as a function of correlation time at different energies for 2D graphene of size 2048×1024 (using 30 random vectors) with defect concentration $n = 1\%$ calculated by the KPM with $N_m = 3000$. For the RECs, the legends “GK”, “E1”, and “E2” refer to Eq. 6, Eq. 9, and Eq. 11, respectively.

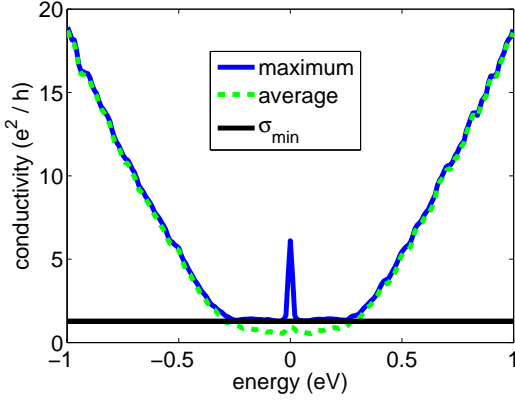


Figure 6: (Color online) Semi-classical conductivity of 2D graphene of size 2048×1024 (using 30 random vectors) with defect concentration $n = 1\%$ calculated by Eq. (53) (labeled by “maximum”) and Eq. (55) (labeled by “average”), using $\sigma^{\text{GK}}(E, t)$. The horizontal line denotes the value of $\sigma_{\text{min}} = 4e^2/(\pi\hbar)$.

value of $\sigma_{\text{sc}}(E)$. Alternatively, we define $\sigma_{\text{sc}}(E)$ as the average value over an appropriate time block $t_1 \leq t \leq t_2$:

$$\sigma_{\text{sc}}(E) = \frac{1}{t_2 - t_1} \int_{t_1}^{t_2} \sigma^{\text{GK}}(E, t) dt. \quad (55)$$

The time block should be chosen to represent the plateau to which $\sigma^{\text{GK}}(E, t)$ saturates to before the onset of localization. This kind of averaging has been widely used in the study of thermal conductivity using the Green-Kubo method [39, 41]. Using this alternative definition, the calculated $\sigma_{\text{sc}}(E)$ (the dashed line in Fig. 6) does not show a peak value around the Dirac point, and is consistent with that obtained by Eq. (53) in the range of $|E| > 0.25$ eV.

The existence of the peak for semi-classical conductivity is also not supported by the work of Ferreira *et al.* [42]. They directly evaluate the Kubo-Greenwood formula (Eq. (2)) by expanding both of the δ -functions using the KPM [43]. Since the KPM is equivalent to the FTM, as demonstrated earlier, their method is also equivalent to Fourier transforming both of the δ -functions,

$$\sigma^{\text{KG}}(E) \approx \frac{e^2(\Delta\tau)^2}{2\pi\hbar\Omega} \sum_{n=-N_m}^{N_m} \sum_{k=-N_m}^{N_m} w_n w_k e^{iE(n+k)\Delta\tau/\hbar} F_{nk}^{\text{VAC}}, \quad (56)$$

$$F_{nk}^{\text{VAC}} \approx \langle \phi | U(n\Delta\tau) V U(k\Delta\tau) V | \phi \rangle, \quad (57)$$

which is in turn equivalent to applying an extra window function on the VAC before integrating it up to a given correlation time (proportional to N_m) in the Green-Kubo formalism. The extra window function (or damping factor, in the context of the KPM) suppresses the localization effect and this direct method provides a more unambiguous way of determining the semi-classical conductivity. Our new definition of $\sigma_{\text{sc}}(E)$ is more or less equivalent to this direct method.

5.3. The localized transport regime

Although the Green-Kubo formula and the Einstein formula have been demonstrated to be equivalent, we should point out that the Green-Kubo formula is not practical in the localization regime, for the reason presented below. To obtain the REC by integrating the VAC, the time step should be very small; otherwise, the integration cannot be accurately evaluated with even very small fluctuations in the VAC data. However, observing localization requires a very long total correlation time, and a large number of steps when using a small time step. At each time step, we need to calculate the δ function, which is very time-consuming. Thus, the necessity of using a small time step in the Green-Kubo formula makes it impractical in the localized regime. This probably explains why the results obtained by integrating (or summing) the VAC show no evidence of localization even for a relatively high (5%) level of resonant disorder [23, 42]. In contrast, the Einstein formula is more suitable for studying the localization behavior, since the numerical evaluation of the derivative-based REC does not require a small time step. We thus only use the Einstein formula in the following discussions of localization.

We begin with a comparison of the results obtained by the Einstein formula with those by the non-equilibrium Green’s function (NEGF) method [1]. To our knowledge, a serious comparison of the two methods in the strongly localized regime is still absent. We consider AGNRs with a fixed width ($W = 12$ nm) and a defect concentration of $n = 1\%$. In the NEGF method, the lengths are set by imposing two conducting leads along the transport direction. In the Einstein formula, we take a sample size of 95×32768 (which is long enough to eliminate any finite size effect in the transport direction) and calculate the lengths by Eq. (50).

Due to the efficiency of our GPU implementation, we can explore the strongly localized regime by cheaply calculating the correlation function up to hundreds of picoseconds for the first time, eventually observing the saturation of the MSD. When the MSD saturates, small fluctuations of the MSD can cause large fluctuations of the REC, $\sigma^{\text{E1}}(E, t)$. Fortunately, we note that the later part of the MSD can be fitted very well by a Padé approximant of order $[m/n]$:

$$\Delta X^2(E, t) = \frac{\sum_{j=0}^m a_j t^j}{1 + \sum_{k=0}^n b_k t^k}. \quad (58)$$

Usually, $m = n = 2$ is enough to obtain a good fitting. An example of the fitting is shown in Fig. 7 (a) for the energy $E = 0.3$ eV.

Without fitting, the REC $\sigma^{\text{E1}}(E, t)$ calculated by Eq. (9) can even develop negative values. In contrast, the REC $\sigma^{\text{E2}}(E, t)$ calculated by Eq. (11) exhibits a very smooth behavior even by using the raw data of the MSD (Fig. 7 (b)). In fact, there is no noticeable difference between the fitted and the raw data when using the division-based definition $\sigma^{\text{E2}}(E, t)$. However, in the strongly localized regime where $\sigma \ll e^2/h$, the two definitions can lead to a difference of several orders of magnitude for the conductivity (Fig. 7 (b)).

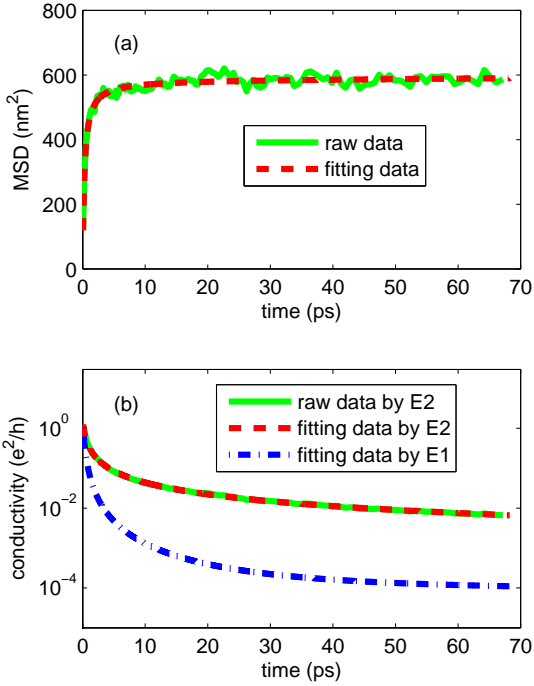


Figure 7: (Color online) Transport properties of AGNR of size 95×32768 (using 12 random vectors) with defect concentration $n = 1\%$ at $E = 0.3$ eV. (a) Raw and fitted MSD as a function of correlation time. (b) Conductivity as a function of correlation time. Data marked by E1 and E2 correspond to $\sigma^{E1}(E, t)$ defined by Eq. (9) and $\sigma^{E2}(E, t)$ defined by Eq. (11), respectively. For $\sigma^{E2}(E, t)$, results calculated from the raw and the fitted MSD are compared. For $\sigma^{E1}(E, t)$, only the results calculated from the fitted MSD are presented; those from the raw MSD have large fluctuations and cannot be shown completely in the same plot.

With a reliable fitting method for obtaining smooth curves of the MSD and the REC, we can give a quantitative comparison of the length-dependent conductances as calculated by

$$G(E, L) = \frac{W}{L(E, t)} \sigma(E, t) \quad (59)$$

with those calculated by the NEGF method, as shown in Fig. 8. In the NEGF method, the typical conductance [44]

$$G_{\text{typ}}(E, L) = e^{\langle \ln G(E) \rangle} \quad (60)$$

is used to represent the ensemble average over $10^2 - 10^3$ realizations of the defects. As expected, the conductances calculated by the NEGF method decay exponentially with the sample length [44, 45]

$$G_{\text{typ}}(E, L) = G_0(E) e^{-L/\xi(E)}, \quad (61)$$

where $\xi(E)$ is the localization length and $G_0(E)$ the number of transport modes in the ribbon multiplied by the conductance quantum e^2/h . The conductances calculated by the Einstein formula also exhibit an exponential decay up to $G(E, L) \approx 0.1e^2/h$. Within this range, the correct definition of the REC, $\sigma^{E1}(E, t)$, results in a very good agreement between the Einstein formula and the NEGF method. However, for $G(E, L) < 0.1e^2/h$, the Einstein formula fails to capture the length-dependence of the conductance by using either definition of the REC. In this strongly localized regime, the conductances calculated by the Einstein formula decay “super-exponentially” with increasing length.

A better characterization of the range within which the Einstein formalism and the NEGF method give consistent results can be obtained by plotting the conductances as a function of the reduced length $L/\xi(E)$, where the localization length $\xi(E)$ is deduced from the NEGF results. The length definition $L(E, t) = 2\sqrt{\Delta X^2(E, t)}$ in the Einstein formalism can only be trusted within this range. As shown in the insets of Fig. 8, this range can be determined to be $L/\xi(E) < 4$, independent of the energy.

This discrepancy puts the definition of length in the Einstein formalism into question. Indeed, as seen from Fig. 7, the MSD will finally saturate with increasing correlation time, which means that the length defined in Eq. (50) does not increase after the saturation. Thus, the maximum length that can be probed by the Einstein formula is bounded from above. In fact, by solving Eq. (50), Eq. (59), Eq. (9) and Eq. (61) simultaneously, we can get analytical expressions for the length and the MSD:

$$L(E, t) = 2\sqrt{\Delta X^2(E, t)} = L_0(E) \ln\left(\frac{t + t_1}{t_2}\right), \quad (62)$$

where t_1 and t_2 are two positive parameters depending on the energy, and $L_0(E)$ is an energy-dependent length parameter. However, our simulation results do not support this solution: the calculated MSD saturates much faster than logarithmically. Conceptually, one unambiguous way to define the length of a simulated sample is to connect it with two semi-infinite leads

along the transport direction, which affect the effective Hamiltonian of the sample by adding the “self energies” arising from the interactions between the sample and the leads. This inevitably leads to the “mesoscopic Kubo-Greenwood formula” [46–48], or equivalently, the NEGF method [1].

6. Conclusions

In summary, we have developed an efficient quantum transport simulation code fully implemented on the GPU, which attains a speedup factor of 16 (using double-precision) compared with an optimized serial CPU code. This seemingly relatively small speedup factor is obtained by considering the simplest tight-binding model for graphene, with only three off-diagonal elements in each row (or column) of the Hamiltonian. We expect that much higher speedup factors can be obtained when considering more complicated tight-binding models. Only electronic transport has been considered in this work; extension of our GPU implementation to thermal transport [22] should be straightforward and a higher acceleration rate can be expected due to the higher computational intensity resulting from the denser phonon Hamiltonian. Our methods can also be extended to study other properties such as local density of states [49], which serves an alternative method for studying Anderson localization. For the interested reader, our GPU code is available upon request.

Starting from the Kubo-Greenwood formula, we have presented a unified picture of the Green-Kubo formula based on the velocity auto-correlation and the Einstein formula based on the mean square displacement for DC electrical conductivity and demonstrated their equivalence for diffusive transport. We also compared the kernel polynomial method and the Fourier transform method for approximating the δ function and found that they can be equally used but the former is more efficient. The demonstration of the equivalence between the Green-Kubo and the Einstein formula and that between the kernel polynomial method and the Fourier transform method validates our implementation non-trivially.

Using the developed GPU code, we performed a comprehensive evaluation on the applicability of the method by studying transport properties of graphene systems in the ballistic, diffusive and localized regimes. In all the transport regimes, we found that the division-based definition of the conductivity in the Einstein formalism is not equivalent to the correct derivative-based definition, and should be used with caution.

In the ballistic regime, we justified the definition of length in the Einstein formalism: $L(E, t) = 2\sqrt{\Delta X^2(E, t)}$, where $\Delta X^2(E, t)$ is the mean square displacement. We found that the quantized conductance for graphene nanoribbons can be accurately calculated except for the band edges. Around the band edges, the conductance is overestimated. We pointed out that this overestimation arises from the difficulty of correctly calculating the density of states and the velocity, which are both singular around the band edges.

In the diffusive regime, we proposed a new way of finding the semi-classical conductivity and compared it with other

approaches. Especially, we established a connection between our methods and a method which directly evaluates the Kubo-Greenwood formula by expanding both of the δ functions using the kernel polynomial method. Although the Green-Kubo formula is equivalent to the Einstein formula in the diffusive regime, the former is not as practical as the latter in the localized regime. The reason is that the former is based on a time-integration and thus requires a small time step, while the latter is based on a time-derivative and does not require a small time step.

In the localized regime, the Einstein formula can produce results which are consistent with those obtained by the NEGF method up to some critical length, $L < 4\xi(E)$, where $\xi(E)$ is the localization length. Although the definition of length can only be trusted when $L < 4\xi(E)$, in practice, this is enough to observe the weak-to-strong localization transition. More work is needed to clarify the still controversial topics of Anderson localization in graphene.

Acknowledgements

We thank Aires Ferreira, Aurélien Lherbier, Stephan Roche, and Shengjun Yuan for helpful discussions. This research has been supported by the Academy of Finland through its Centres of Excellence Program (project no. 251748).

References

- [1] S. Datta, *Electronic Transport in Mesoscopic Systems*. Cambridge University Press, 1995.
- [2] R. Kubo, *Statistical-Mechanical Theory of Irreversible Processes. I. General Theory and Simple Applications to Magnetic and Conduction Problems*, *J. Phys. Soc. Jpn.* **12**, (1957) 570-586.
- [3] D. A. Greenwood, *The Boltzmann Equation in the Theory of Electrical Conduction in Metals*. *Proc. Phys. Soc.* **71**, (1958) 585-596.
- [4] A. K. Geim and K. S. Novoselov, *The rise of graphene*, *Nature Materials*, **6**, (2007) 183-191.
- [5] A. H. Castro Neto, F. Guinea, N. M. R. Peres, K. S. Novoselov and A. K. Geim, *The electronic properties of graphene*, *Rev. Mod. Phys.*, **81**, (2009) 109-162.
- [6] M. P. L. Sancho, J. M. L. Sancho and J. Rubio, *Highly convergent schemes for the calculation of bulk and surface Green functions*, *J. Phys. F: Met. Phys.* **15** (1985) 851-858.
- [7] D. Mayou, *Calculation of the Conductivity in the Short-Mean-Free-Path Regime*, *Europhys. Lett.* **6**, (1988) 549-554.
- [8] D. Mayou and S. N. Khanna, *A Real-Space Approach to Electronic Transport*, *J. Phys. I Paris* **5**, (1995) 1199-1211.
- [9] S. Roche and D. Mayou, *Conductivity of quasiperiodic systems: a numerical study*, *Phys. Rev. Lett.* **79**, (1997) 2518-2521.
- [10] F. Triozon, J. Vidal, R. Mosseri, and D. Mayou, *Quantum dynamics in two- and three-dimensional quasiperiodic tilings*, *Phys. Rev. B* **65**, (2002) 220202(R).
- [11] F. Triozon, S. Roche, A. Rubio, and D. Mayou, *Electrical transport in carbon nanotubes: Role of disorder and helical symmetries*, *Phys. Rev. B* **69**, (2004) 121410(R).
- [12] T. Markussen, R. Rurali, M. Brandbyge, and A.-P. Jauho, *Electronic transport through Si nanowires: Role of bulk and surface disorder*, *Phys. Rev. B* **74** (2006) 245313.
- [13] H. Ishii, N. Kobayashi, and K. Hirose, *Order- N electron transport calculations from ballistic to diffusive regimes by a time-dependent wave-packet diffusion method: Application to transport properties of carbon nanotubes*, *Phys. Rev. B* **82**, (2010) 085435.

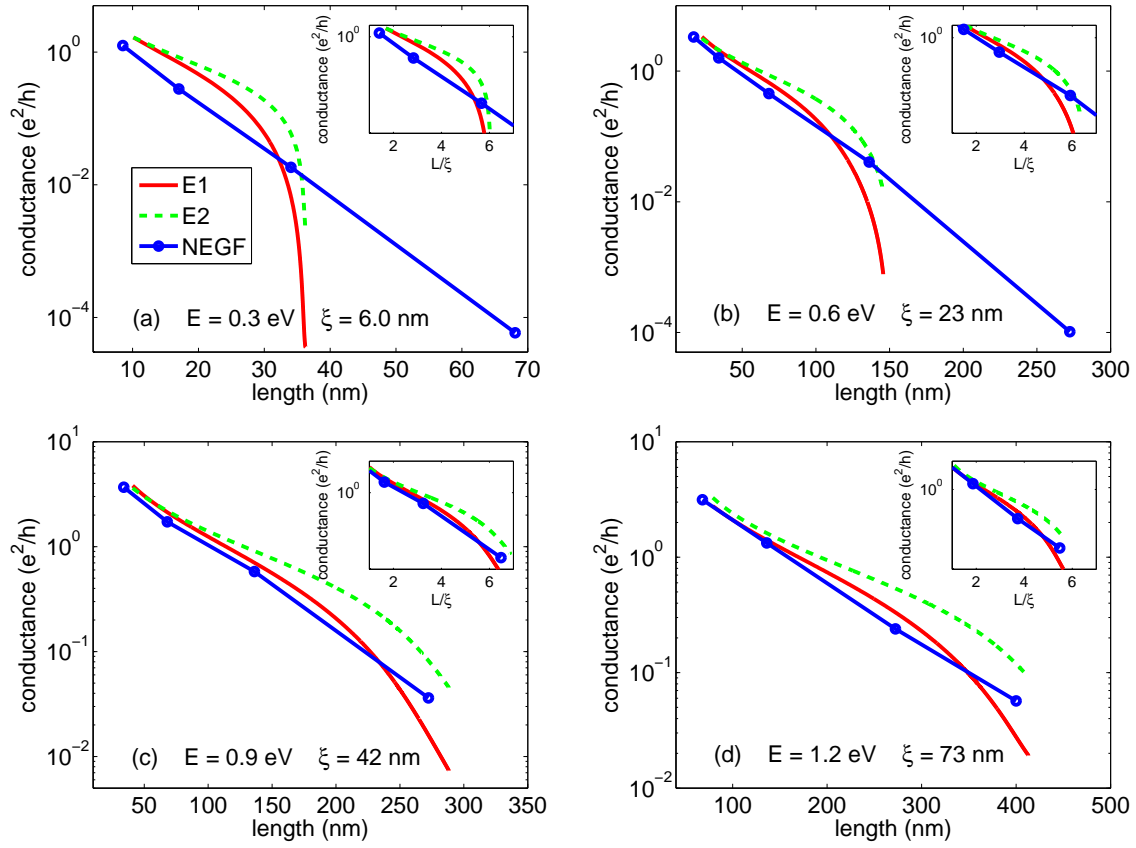


Figure 8: (Color online) Conductance as a function of length $L = 2\sqrt{\Delta X^2(E, t)}$ for AGNR of size 95×32768 (using 12 random vectors) with defect concentration $n = 1\%$ at different energies. Solid lines, dashed lines and lines with symbols correspond to the results obtained by Eq. (9), Eq. (11) and NEGF calculations, respectively. The insets show the conductances as a function of the reduced length $L/\xi(E)$.

- [14] A. Lherbier, B. Biel, Y.-M. Niquet, and S. Roche, Transport Length Scales in Disordered Graphene-based Materials: Strong Localization Regimes and Dimensionality Effects, *Phys. Rev. Lett.* **100**, (2008) 036803.
- [15] A. Lherbier, X. Blase, Y.-M. Niquet, F. Triozon and S. Roche, Charge Transport in Chemically Doped Graphene, *Phys. Rev. Lett.* **101**, (2008) 036808.
- [16] G. T. de Laissardiere and D. Mayou, Electronic transport in graphene: quantum effects and role of local defects, *Modern Physics Letters B*, **25** (2011) 1019-1028.
- [17] N. Leconte, A. Lherbier, F. Varchon, P. Ordejon, S. Roche, and J.-C. Charlier, Quantum transport in chemically modified two-dimensional graphene: From minimal conductivity to Anderson localization, *Phys. Rev. B* **84** (2011) 235420.
- [18] A. Lherbier, S. M.-M. Dubois, X. Declerck, Y.-M. Niquet, S. Roche, and J.-C. Charlier, Transport properties of graphene containing structural defects, *Phys. Rev. B*, **86**, (2012) 075402.
- [19] T. M. Radchenko, A. A. Shylau, and I. V. Zozoulenko, Influence of correlated impurities on conductivity of graphene sheets: Time-dependent real-space Kubo approach, *Phys. Rev. B* **86**, (2012) 035418.
- [20] D. Van Tuan, J. Kotakoski, T. Louvet, F. Ortmann, J. C. Meyer, and S. Roche, Scaling properties of charge transport in polycrystalline graphene, *Nano Lett.* **13**, (2013) 1730-1735.
- [21] A. Cresti, F. Ortmann, T. Louvet, D. Van Tuan, and S. Roche, Broken symmetries, zero-energy modes, and quantum transport in disordered graphene: from supermetallic to insulating regimes, *Phys. Rev. Lett.* **110**, (2013) 196601.
- [22] W. Li, H. Sevinçli, S. Roche, and G. Cuniberti, Efficient linear scaling method for computing the thermal conductivity of disordered materials, *Phys. Rev. B* **83**, (2011) 155416.
- [23] S. Yuan, H. De Raedt, and M. I. Katsnelson, Modeling electronic structure and transport properties of graphene with resonant scattering centers, *Phys. Rev. B*, **82**, (2010) 115448.
- [24] S. Yuan, H. De Raedt, and M. I. Katsnelson, Electronic transport in disordered bilayer and trilayer graphene, *Phys. Rev. B*, **82**, (2010) 235409.
- [25] S. Yuan, R. Roldán, A.-P. Jauho, and M. I. Katsnelson, Electronic properties of disordered graphene antidot lattices, *Phys. Rev. B*, **87**, (2013) 085430.
- [26] A. Harju, T. Siro, F. Federici-Canova, S. Hakala, and T. Rantalaiho, Computational Physics on Graphics Processing Units, *Lecture Notes in Computer Science*, **7782**, (2013) 3-26.
- [27] M. S. Green, Markoff Random Processes and the Statistical Mechanics of Time-Dependent Phenomena. II. Irreversible Processes in Fluids, *J. Chem. Phys.* **22** (1954) 398-413.
- [28] A. Weiße, G. Wellein, A. Alvermann, and H. Fehske, The kernel polynomial method, *Review of Modern Physics*, **78**, (2006) 275-306.
- [29] R. Haydock, V. Heine and M. J. Kelly, Electronic structure based on the local atomic environment for tight-binding bands, *J. Phys. C: Solid State Phys.* **5**, (1972) 2845-2858.
- [30] R. Haydock, V. Heine and M. J. Kelly, Electronic structure based on the local atomic environment for tight-binding bands. II, *J. Phys. C: Solid State Phys.* **8**, (1975) 2591-2605.
- [31] M. D. Feit, J. A. Fleck, Jr., and A. Steiger, Solution of the Schrödinger Equation by a Spectral Method, *Journal of Computational Physics*, **47**, (1982) 412-433.
- [32] A. Hams and H. De Raedt, Fast algorithm for finding the eigenvalue distribution of very large matrices, *Phys. Rev. E*, **62**, (2000) 4365-4377.
- [33] H. Tal-Ezer and R. Kosloff, An Accurate and Efficient Scheme for Propagating the Time Dependent Schrödinger Equation, *J. Chem. Phys.* **81**, (1984) 3967-3971.
- [34] H. Fehske, J. Schleede, G. Schubert, G. Wellein, V. S. Filinov, and A. R. Bishop, Numerical approaches to time evolution of complex quantum systems, *Physics Letters A* **373**, (2009) 2182-2188.
- [35] T. Dziubak and J. Matulewski, An object-oriented implementation of a solver of the time-dependent Schrödinger equation using the CUDA technology, *Computer Physics Communications*, **183** (2012) 800-812.
- [36] C. Ó Broin, and L. A. A. Nikolopoulos, An OpenCL implementation for the solution of the time-dependent Schrödinger equation on GPUs and CPUs, *Computer Physics Communications*, **183**, (2012) 20712080.
- [37] T. Siro and A. Harju, Time Propagation of Many-Body Quantum States on Graphics Processing Units, *Lecture Notes in Computer Science*, **7782**, (2013) 141-152.
- [38] NVIDIA, CUDA Programming Guide, version 5.0 (2013).
- [39] Z. Fan, T. Siro, and A. Harju, Accelerated molecular dynamics force evaluation on graphics processing units for thermal conductivity calculations, *Computer Physics Communications*, **184**, (2013) 1414-1425.
- [40] T. Siro, A. Harju, Exact diagonalization of the Hubbard model on graphics processing units, *Computer Physics Communications*, **183** (2012) 1884-1889.
- [41] P. K. Schelling, S. R. Phillpot, and P. Keblinski, Comparison of atomic-level simulation methods for computing thermal conductivity, *Phys. Rev. B* **65** (2002) 144306.
- [42] A. Ferreira, J. Viana-Gomes, J. Nilsson, E. R. Mucciolo, N. M. R. Peres, and A. H. Castro Neto, Unified description of the dc conductivity of monolayer and bilayer graphene at finite densities based on resonant scatterers, *Phys. Rev. B* **83**, (2011) 165402.
- [43] Private communication with A. Ferreira.
- [44] P. W. Anderson, D. J. Thouless, E. Abrahams, and D. S. Fisher New method for a scaling theory of localization *Phys. Rev. B* **22**, (1980) 3519.
- [45] A. Uppstu, K. Saloritta, A. Harju, M. Puska, and A.-P. Jauho, Electronic transport in graphene-based structures: An effective cross-section approach *Phys. Rev. B* **85**, (2012) 041401(R).
- [46] D. S. Fisher and P. A. Lee, Relation between conductivity and transmission matrix, *Phys. Rev. B* **23**, (1981) 6851-6854.
- [47] J. A. Vergés, Computational implementation of the Kubo formula for the static conductance: application to two-dimensional quantum dots, *Computer Physics Communications*, **118**, (1999) 71-80.
- [48] B. K. Nikolić, Deconstructing Kubo formula usage: Exact conductance of a mesoscopic system from weak to strong disorder, *Phys. Rev. B* **64**, (2001) 165303.
- [49] G. Schubert, J. Schleede, and H. Fehske, Anderson disorder in graphene nanoribbons: A local distribution approach, *Phys. Rev. B* **79**, (2009) 235116.